FRONTIERS OF PHYSICS

RESEARCH ARTICLE
Volume 19 / Issue 4 / 43200 / 2024

Room-temperature ferromagnetism and half-metallicity in monolayer orthorhombic CrS_2

Bocheng Lei (雷博程)[1,3], Aolin Li (李奥林)[1,†], Wenzhe Zhou (周文哲)[2], Yunpeng Wang (王云鹏)[2], Wei Xiong (熊威)[1], Yu Chen (陈羽)[2], Fangping Ouyang (欧阳方平)[1,2,4,‡]

1 School of Physics Science and Technology, and Xinjiang Key Laboratory of Solid-State Physics and Devices, Xinjiang University, Urumqi 830046, China
2 School of Physics, and Hunan Key Laboratory for Super-Microstructure and Ultrafast Process, and Hunan Key Laboratory of Nanophotonics and Devices, Central South University, Changsha 410083, China
3 School of Physics Science and Technology, and Xinjiang Laboratory of Phase Transitions and Microstructures in Condensed Matter Physics, Yili Normal University, Yining 835000, China
4 Powder Metallurgy Research Institute and State Key Laboratory of Powder Metallurgy, Central South University, Changsha 410083, China
Corresponding authors. E-mail: †liaolin628@xju.edu.cn, ‡ouyangfp06@tsinghua.org.cn
Received October 11, 2023; accepted January 9, 2024

ABSTRACT

Two-dimensional materials with high-temperature ferromagnetism and half-metallicity have the latest applications in spintronic devices. Based on first-principles calculations, we have investigated a novel two-dimensional CrS_2 phase with an orthorhombic lattice. Our results suggest that it is stable in dynamics, thermodynamics, and mechanics. The ground state of monolayer orthorhombic CrS_2 is both ferromagnetic and half-metallic, with a high Curie temperature of 895 K and a large spin-flipping gap on values of 0.804 eV. This room-temperature ferromagnetism and half-metallicity can maintain stability against a strong biaxial strain ranging from –5% to 5%. Meanwhile, increasing strain can significantly maintain the out-of-plane magnetic anisotropy. A density of states analysis, together with the orbital-resolved magnetic anisotropy energy, has revealed that the strain-enhanced MAE is highly related to the 3d-orbital splitting of Cr atoms. Our results suggest the monolayer orthorhombic CrS_2 is an ideal candidate for future spintronics.

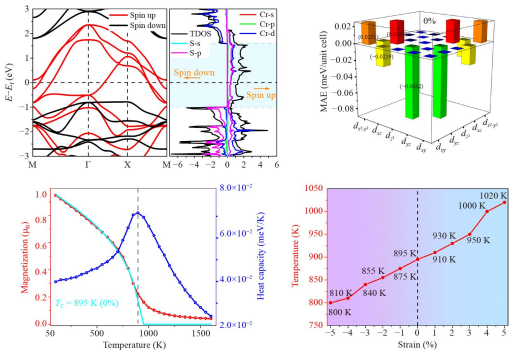

Keywords orthorhombic CrS_2, Curie temperature, magnetic anisotropy energy, biaxial strain, first-principles calculations

1 Introduction

Since the successful preparation of graphene in 2004 [1], numerous two-dimensional (2D) materials have been discovered, such as h-BN [2], transitional metal dichalcogenides (TMDs) [3, 4], phosphorene [5], and MXenes [6], showing novel properties in electronics and spintronics. The well-known Mermin–Wagner theorem [7, 8] indicates spontaneous magnetization cannot exist in 2D isotropic Heisenberg ferromagnets. Therefore, 2D magnetic materials for spintronics have not appeared until recent years, such as CrI_3 [9, 10], Fe_3GeTe_2 [11, 12], and $Cr_2Ge_2Te_6$ [13, 14]. However, most 2D ferromagnets have limited their practical applications due to their low Curie temperature (T_C), and lack of ferromagnetic (FM) order [15, 16]. To overcome these limitations, researchers have

https://doi.org/10.1007/s11467-023-1387-y

identified a class of magnetic half-metallic materials that have the advantages of 100% spin polarizability at the Fermi level, additional carriers to stabilize the long-range magnetic order, and high magnetic moments [17–20]. Therefore, in the development of 2D magnetic devices, researchers have focused on materials with these properties.

According to experimental and theoretical reports, chromium-based magnetic materials have the potential to achieve a high T_C and half-metallicity. For example, researchers synthesized a monolayer of 1T (1T'/2H)-CrS_2 using chemical vapor deposition [21–25]. They have found that 2H-CrS_2 is a nonmagnetic (NM) direct band gap semiconductor, while 1T and 1T'-CrS_2 are metallic and half-metallic ferromagnets [21, 23]. Other researchers discovered that adjusting the thickness of 1T-$CrTe_2$ (8 nm [22], 4 monolayer [24], 7 monolayer [25]) films could result in room temperature ferromagnetism and perpendicular magnetic anisotropy (PMA), and their T_C decreased as thickness lower [24, 25]. Theoretical studies have revealed that 2D CrX_2 (X = O, S, Se, Te) systems exhibit a variety of electronic and magnetic properties, especially in the 1T, 1T', and 2H phases. For instance, CrO_2 in the 2H phase is NM, and the 1T phases are FM and half-metallicity [26, 27]. In the ground state of the CrS_2 [28, 29] and $CrSe_2$ [30, 31] systems, the 2H phase is in the NM state, 1T phase is antiferromagnetic (AFM) state, and 1T' phase is FM state. Conversely, the 1T phase of $CrTe_2$ [32, 33] in the ground state exhibits long-range FM order in the monolayer limit. It is important to note that the T_C reaches 1358 K for 1T'-CrS_2 [29] with 6% uniaxial strain and 110 K for 1T-$CrSe_2$ with 10.8-nm-thick [34]. Chromium tellurium compounds ($Cr_{1+\delta}Te_2$) exhibit a wide range of magnetic order temperatures [35–37] (Cr_3Te_4 = 340 K, Cr_4Te_5 = 318 K, and CrTe = 367 K). These findings raise the question of whether there are other CrX_2 materials with similar structures.

In this work, we have predicted a novel monolayer orthorhombic CrS_2 (ML O-CrS_2) and investigated its electronic structure, magnetic anisotropy energy (MAE), and biaxial strain tunable T_C by using first-principles calculations. The results show that ML O-CrS_2 is FM and a spin-up channel half-metallic with a high T_C (895 K) and MAE (0.034 meV/Cr). Interestingly, the biaxial strain does not change ferromagnetism and half-metallicity and can increase the T_C. The physical mechanism of the magnetic easy axis is explored from the view of atom- and orbit-resolved MAE, which shows that the strong spin–orbit coupling (SOC) introduced by the heavy magnetic Cr atoms plays a crucial role. Our investigations enrich the family of 2D FM materials and may contribute to future experimental studies of novel 2D magnets with high T_C.

2 Calculation method

First-principles calculations were guided by Density Functional Theory (DFT) and implemented in the Vienna Ab initio Simulation Package (VASP) [38, 39]. The exchange-correlation potential was characterized using the Generalized Gradient Approximation (GGA) within the framework of Perdew–Burke–Ernzerh (PBE) formalism. The Projector Augmented Wave (PAW) [40] potential was used to investigate the electron–ion interactions, setting a cutoff energy of 500 eV for ML O-CrS_2. Structural optimizations were performed via the conjugate gradient method, with the convergence criteria set at 10^{-5} eV for the total energy and 0.01 eV/Å for force. The Brillouin zones were sampled using a Gramma-centered Monkhorst–Pack [41] k-point mesh with a grid of 7 × 7 × 1 for structural optimizations, then followed by calculations of electronic and magnetic properties using a 9 × 9 × 1 grid. Periodic boundary conditions were applied in all three directions, and a vacuum space of 20 Å was established along the Z-direction to screen interactions between adjacent layers. The Hubbard U correction was applied to compensate for the strong correlation of the 3d electrons in transition metal Cr atoms, with an effective U_{eff} ($U_{\text{eff}} = U - J$) set to 3.0 eV, as validated in prior studies [21, 42]. The phonon dispersion spectrum was derived using the finite displacement method on a 4 × 4 × 1 supercell via the PHONOPY package [43]. The thermodynamic stability was verified through Ab Initio Molecular Dynamics (AIMD) simulations conducted in the fixed particle number-volume-temperature (NVT) ensemble, with temperature control achieved through a Nosé–Hoover thermostat [44].

3 Results and discussion

3.1 Structure and stability

As shown in Fig. 1(a), the ML O-CrS_2 is stacking by the S–Cr–S sandwich layers along the Z-direction. Its primitive cell belongs to the P-4m2 (No.115) space group (see red rectangular area). Each Cr^{4+} cation is surrounding by six neighboring S^{2-} anions with octahedral coordination. The magnetic properties of the 1T and 1H phases are also calculated, and the results closely align with those observed in previous research [28, 29], thereby confirming the validity of our chosen calculational parameters. Furthermore, Table 1 presents the optimized lattice and magnetic parameters.

To determine the dynamic stability of the ML O-CrS_2, we calculated its phonon spectrum, as shown in Fig. 1(b). The phonon dispersion exhibits a small imaginary frequency around the Γ point (0.2 THz), which can considered as a negligible numerical noise. This indicates ML O-CrS_2 is dynamically stable. We have further performed AIMD simulations, as shown in Fig. 1(c). The

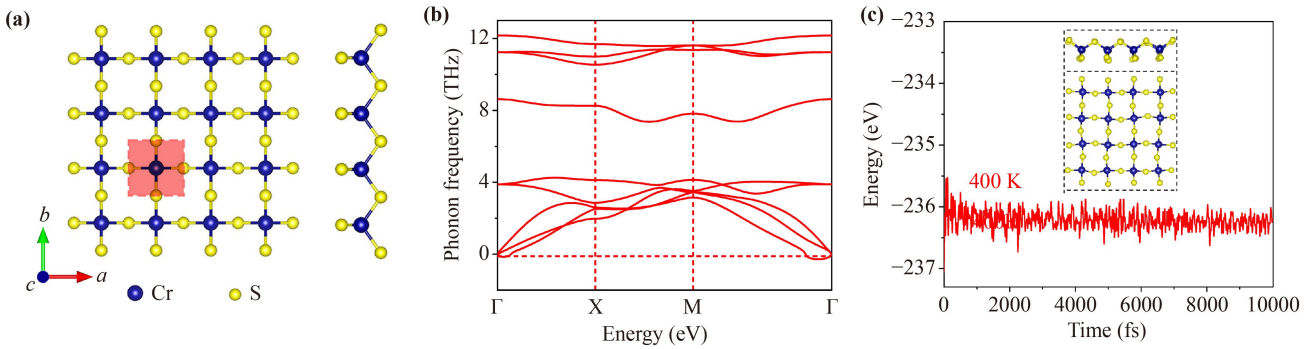

Fig. 1 **(a)** Top and Side views of a completely relaxed 4 × 4 supercell of ML O-CrS_2. The primitive cell is shown in the red square, the blue (yellow) spheres indicate Cr (S) atoms. **(b)** Phonon spectrum without obviously imaginary frequencies. **(c)** Variation of total potential energy E_0 during AIMD simulation at 400 K, and the inset shows the corresponding snapshots of structures at the end of 10 ps.

Table 1 Lattice constants a and b, MAE (meV) per Cr in different directions against the minimum energy spin orientation, exchange energy ΔE (eV), single-atom magnetic moment M (μ_B) in the FM state.

CrS_2	$a = b$ (Å)	E_{100}	E_{010}	E_{001}	ΔE	M_{Cr}	M_{S1}	M_{S2}
1O	3.660	0	0	–0.034	1.912	2.985	–0.371	–0.403
1T	3.290	0	0	–0.086	–0.013	2.588	–0.155	–0.234
	3.280[29]	–	–	–	–0.063	2.664	–0.042	–
1H	3.041	–	–	–	0	0	0	0
	3.041[28]	–	–	–	0	0	0	0

crystal structure remains stable at 400 K for a duration of 10 ps and shows no distinct structural distortion, suggesting ML O-CrS_2 is thermally stable above room temperature. We then calculated the elastic constant tensor of a symmetric 6 × 6 matrix. The elastic constants are $C_{11} = C_{22} = 108.7$ N/m, $C_{12} = 17.4$ N/m, and $C_{66} = 12.8$ N/m, and satisfy the Born criterion of stability [45] ($C_{11} > 0$, $C_{66} > 0$, and $C_{11}\ C_{22} > C_{12}\ C_{12}$), confirming the ML O-$CrS_2$ is mechanically stable.

3.2 Electronic properties

Figure 2 displays the spin-polarized electronic structure of ML O-CrS_2. The band of the spin-up channel crosses the Fermi level, while the spin-down channel band gap is 2.626 eV (see light blue area). The ML O-CrS_2 shows metallicity in the spin-up channel and semiconducting behavior in the spin-down channel. Thus, it exhibits intrinsic half-metallicity. Using the HSE06 hybrid functional and PBE method (see Supplementary Materials Fig. S1), ML O-CrS_2 still exhibits FM and half-metallicity, which is consistent with the results of PBE+U. This suggests that charge transport is fully controlled by bands in the same spin-up channel, resulting in 100% spin-polarization. Therefore, it may serve as an ideal material for spin injection [18, 20]. The spin-flip band gap refers to the minimum energy value in the bottom of spin-down conduction band with respect to the Fermi level and the absolute value of the top energy of spin-

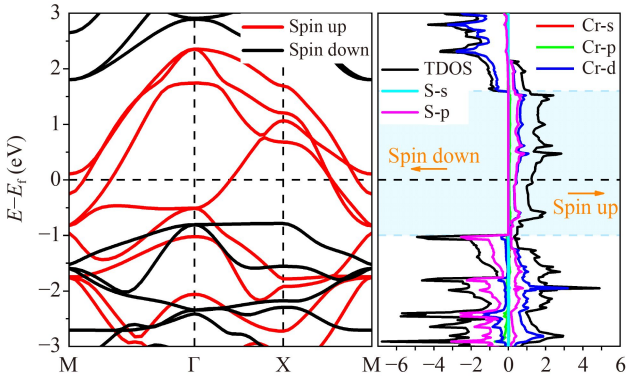

Fig. 2 The electronic structure of ML O-CrS_2 under FM with orange arrows indicating spin-up or spin-down channel.

down valence band [46, 47]. Interestingly, there is a significant spin-flipping gap of 0.804 eV. This particular characteristic allows for the transition from a spin-up excited state to a spin-down state at room temperature while still maintaining a stable spin polarization and remaining unaffected by thermal excitation. As a result, it proves valuable as a critical component in various spintronic devices, including sources and sinks of spin-polarized current, spin-polarized electron memory, and spin field-effect transistors [14, 19, 42]. Within the energy range from –3 to 2 eV, the Cr-3d and S-3p orbitals exhibit a significant overlapping peak, indicating considerable orbital hybridization.

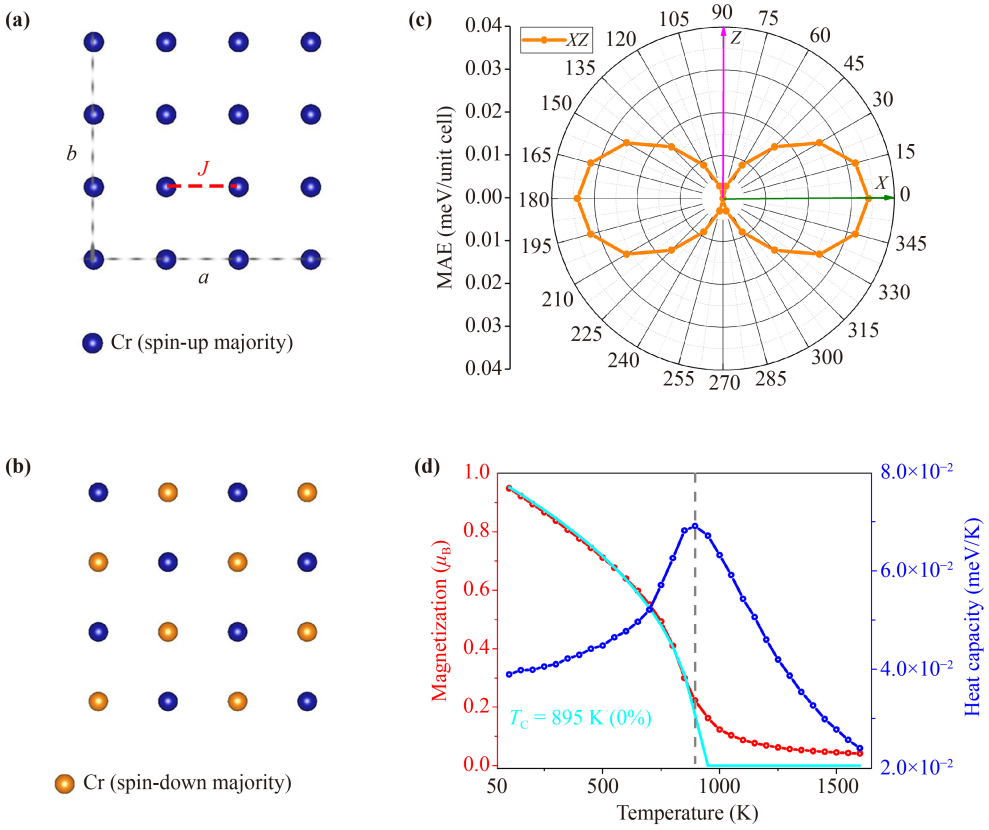

Fig. 3 The magnetic configurations of ML O-CrS_2 within 4 × 4 supercell, as shown in **(a)** and **(b)**. The blue (yellow) spheres represent the majority spin-up (-down) states. The lattice constants a and b are denoted by gray dashed lines, while the J between the nearest-neighbor Cr atoms is indicated by a red dashed line. **(c)** The energy variation of the magnetic anisotropy in the XZ plane. **(d)** The evolution of total magnetization and specific heat of ML O-CrS_2, obtained from MC simulation, with the fitting results are represented by cyan lines.

3.3 Magnetic properties

The spin Hamiltonian can be expressed as

$$H = H_0 + \left[-\frac{J}{2}\sum_{ij} S_i S_j + \sum_i A_e (S_i^e)^2\right], \quad (1)$$

$$J = \frac{E_{\mathrm{AFM}} - E_{\mathrm{FM}}}{16S^2}. \quad (2)$$

Here, H and H_0 represent the Hamilton and nonmagnetic energy, respectively. J represents the nearest-neighbor Heisenberg exchange parameter. To simplify the calculation, S_iS_j represents the spin state of Cr atom in i/j cite, S is taken as normalized, and the term with A represents the easy-axis single-ion magnetic anisotropy. E_{FM} and E_{AFM} represent the FM and AFM energy, respectively.

To determine the magnetic ground state, we have analyzed potential magnetic configurations, including NM, FM, and AFM order [see Figs. 3(a) and (b)]. For the ML O-CrS_2 system, the FM state energy is lower than that of the AFM state, regardless of the adopted function. The FM state remains stable even at six different values of U (0–5 eV, see Supplementary Materials Tables S1 and S2). The spin-charge density further proves that the magnetism mainly originates from the Cr element and partially from the S element (see Supplementary Materials Fig. S2). The spin polarization of S is opposite to that of Cr, which favors an FM coupling between Cr sites, which is consistent with results obtained from Fig. 2. The spin exchange parameter (J) was calculated value of 119.519 meV. The PBE, PBE+U, and HSE06 functions have shown a positive J, indicating the presence of FM state in the ML O-CrS_2 (see Supplementary Materials Table S1).

To evaluate the angle-dependent MAE, we conducted noncollinear magnetic calculations considering the influence of SOC. Figure 3(c) illustrates the MAE of ML O-CrS_2 when the magnetization angle is limited to the XZ plane (the X and Y plane being equivalent). The MAE is determined by the energy difference between an arbitrary magnetization direction and a specific one (MAE = E_{001}–E_{100}). In ML O-CrS_2, the magnetic easy axis is out-of-plane (Z axis), while the in-plane represents the magnetic hard axis. The SOC effect in 2D systems significantly contributes to the MAE, with Cr, a heavy

element, exhibiting a strong SOC effect. This could account for the observed large MAE. The intensity of MAE magnetization is 0.034 meV/Cr, which is comparable to that of 1T-CrO_2 [27] and FeP_4 [20]. The presence of MAE ensures the stable existence of the FM state at higher temperatures by resisting thermal disturbance.

Next, we analyze the microscopic mechanism underpinning the ferromagnetism in the CrS_2 system. Our calculations reveal that the Cr-3d orbitals primarily contribute to the total magnetic moments, and the contribution of S element is negligible. To understand the strong FM coupling in monolayer O-CrS_2, there are three prevalent mechanisms should be considered: direct and super-exchange interactions induced by the coupling of local magnetic moments, and the itinerant electron magnetism originating from the half-metallicity. We first consider the direct exchange coupling mechanism. The nearest-neighbor distance between Cr atoms is 3.66 Å, approaching the sum of radii of two Cr atoms (3.70 Å). As a comparison, monolayer $CrCl_3$ should very weakly AFM coupling due to the direct exchange coupling [48], which has a Cr–Cr distance of 3.49 Å slightly smaller than that of monolayer O-CrS_2. A larger distance will further weaken the direct exchange coupling, therefore it should be fractional in monolayer CrS_2. Then we consider the super-exchange mechanism. Typically, the crossover angle from FM to AFM coupling is 127° ± 0.6° for the super-exchange coupling between half-occupied 3d-orbitals [49], the Cr–S–Cr bond angle of 109.66° is inclined towards FM. According to the findings of Soriano *et al.* [48], the Cr–I–Cr bond angle in CrI_3 is 97.5°, which is characteristic of the FM super-exchange, and the Mo–I–Mo bond angle in MoTeI is 113.43°, which also belongs to FM super-exchange [50]. This suggests that the FM super-exchange in the monolayer O-CrS_2 may be more favorable and is not expected to be particularly strong. It is noteworthy that the CrS_2 system exhibits half-metallicity, a characteristic commonly observed in other metallic systems such as Fe_3GeTe_2 [51], FeTe [52], and 1T-$CrTe_2$ [23], which are known to exhibit strong ferromagnetism. This observation suggests that itinerant electromagnetism is instrumental in achieving robust FM exchange interactions. By calculating the densities of states for NM, FM, and AFM configurations (see Supplementary Materials Fig. S7), we observe a reduction in their distributions near the Fermi surface. This indicates a tendency for the system's energy to decrease in the FM state. For the first, second, and third nearest-neighboring Cr–Cr pairs, the exchange parameters can be estimated as J_1 = 119.519 meV, J_2 = 4.471 meV, and J_3 = –9.097 meV, respectively, as FM coupling interactions. Therefore, the FM coupling in the monolayer O-CrS_2 primarily originates from itinerant ferromagnetism.

Based on the classical Heisenberg model, the Monte Carlo (MC) method [53] with the Metropolis algorithm is used to analyze the thermal dynamics of magnetism in the equilibrium state. All the renormalization group MC algorithms described here were executed in the open-source project Spirit package [54]. Figure 3(d) presents the calculated magnetization and specific heat as a function of temperature. The T_C is estimated to be 895 K, and the magnetization curves are well-fitted by using the Curie–Bloch equation [55] in the classical limit (cyan lines). Its T_C is far higher than the experimental results of other 2D FM materials like CrI_3 (45 K) [10] and $CrTe_2$ (200 K) [25]. In terms of its theoretical value, its T_C is also higher than that of other monolayers like 1T-$CrTe_2$ (405 K) [32] and lepidocrocite-type CrS_2 (842 K) [42]. The results suggest the presence of ferromagnetism with T_C above room temperature exists in ML O-CrS_2. To verify the T_C, we employed the same method to simulate a hexagonal lattice ML CrI_3 (see Supplementary Materials Fig. S4), which yielded a T_C value of 55 K, almost consistent with previous experimental works [10].

3.4 Strain engineering

In this work, we explored the relations for the ML O-CrS_2 under the biaxial strain along the XY-plane, which is defined as: $\varepsilon_{xy} = (a - a_0)/a_0 \times 100\%$. Here, a and a_0 represent the in-plane lattice constants for strained and unstrained monolayers, respectively. The calculated results show that the FM configuration is the ground state of the ML O-CrS_2 with net magnetic moments per unit cell close to $2\mu_B$. Further analysis revealed that the FM energy is consistently lower than the AFM energy, indicating that the system maintains good FM properties (see Supplementary Materials Fig. S5). The Cr ions carry most of the magnetic moment, while the adjacent S ions exhibit AFM spin polarization (see Supplementary Materials Table S3). The ML O-CrS_2 has an exchange energy [ΔE = (E_{AFM} – E_{FM}) / unit cell] of 1.738 (2.176) eV for –5 (5)%. As a result of increasing distances between adjacent Cr–Cr, ΔE monotonically increases with strain growth, indicating that the system remains FM.

To develop practical spintronic devices with half-metallic ferromagnets, the half-metallic gap should be wide enough to prevent them from spin-flip transitions caused by thermal disturbance and maintain half-metallicity at room temperature. Half-metals can exhibit three energy gaps. The spin-flip gap $\Delta1(\Delta3)$ is defined as the absolute value of the top(bottom) energy of spin-down valence(conduction) band with relative to the Fermi level. The spin-flip gap $\Delta2$ represents the spin-down channel band gap [46, 47]. In Fig. 4(a), when biaxial strain increases, spin-flip gap $\Delta1$ and $\Delta2$ increase significantly, while $\Delta3$ increases slightly. Under 5% tensile strain, the band gap $\Delta2$ is 3.026 eV, which is about 137.8% of that under the –5% compressive strain (2.195 eV), indicating that biaxial strain can significantly increase the spin-flip gap of the system. We analyzed

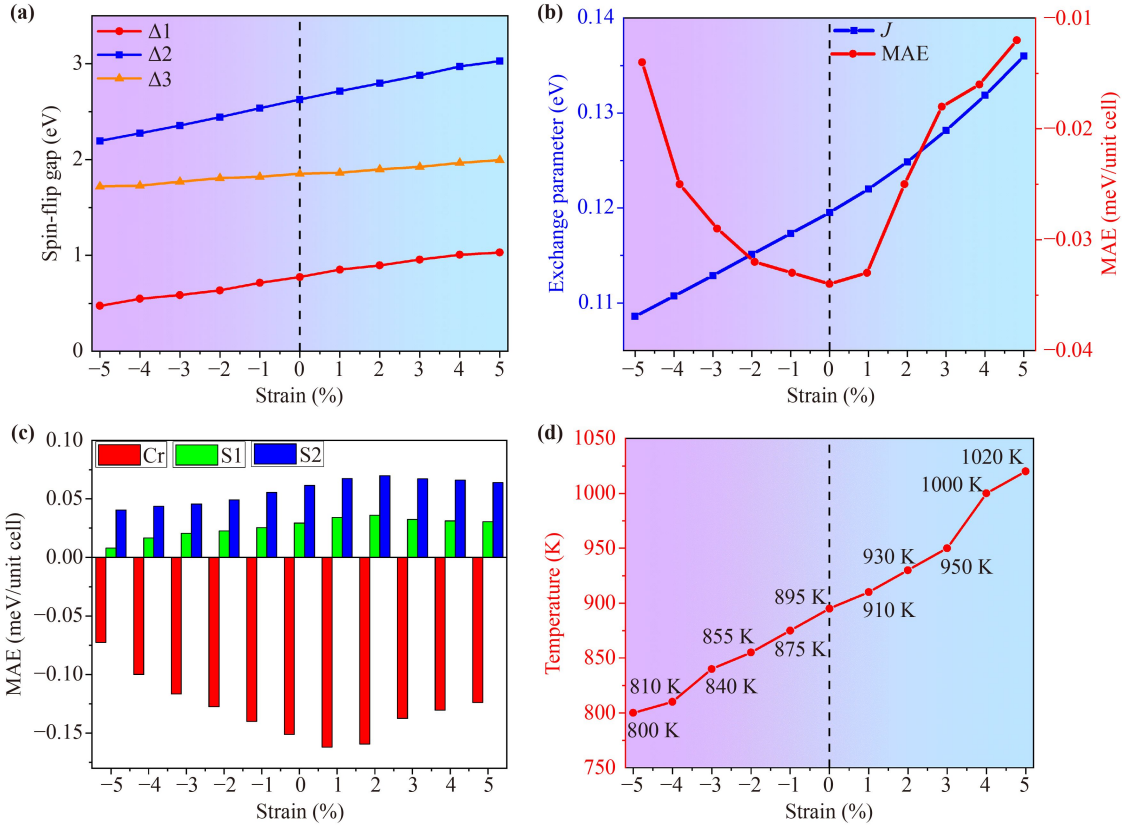

Fig. 4 The properties of ML O-CrS_2 under biaxial strain. **(a)** The spin-flip gap. **(b)** The variation curves of J (blue line) and MAE (red line). **(c)** The atom-resolved MAE. **(d)** The change of T_C.

the spin-polarized energy band structure of the ML O-CrS_2 to investigate its electronic property (see Supplementary Materials Fig. S6 and Table S3). The band of the spin-up (spin-down) channel gradually move as the biaxial strain changes. The biaxial strain in the range from –5% to 5% does not change energy band structure properties, and the band minimum of the spin-down channel is always localized at the high-symmetry M-point due to the strong localization effect of the 3d orbital of the transition metal Cr atom, maintaining FM in spin-up channel half-metallicity.

Figure 4(b) illustrates the J and MAE function under biaxial strain. A consistent increase in J with strain is observed (see Supplementary Materials Table S4). At a compressive strain of –5%, the value of J is 0.108 eV, which can increase up to 0.136 eV at a tensile strain of 5%. This indicates a 25% increase, suggesting that the T_C of the intrinsic ML O-CrS_2 system [e.g., Fig. 4(d)] is also likely to increase. For practical device applications, external tuning of the MAE is crucial. We further discovered that the MAE is sensitive to both biaxial strain and energy, its minimum in the unstrained state. Additionally, the magnetization easy axis consistently remains out-of-plane (Z axis), and biaxial strain does not alter the magnetization easy axis. The MAE significantly decreases with increasing compressive strain, while a similar trend is observed for tensile strain. This suggests that biaxial strain can significantly adjust the MAE. To comprehend why biaxial strain can enhance the PMA for ML O-CrS_2, we initially analyzed the atom-resolved MAEs. As depicted in Fig. 4(c), the MAE is primarily contributed by the Cr and S atoms. There is a notable shift in the contribution from S1(S2) atoms towards a more positive MAE, while the contribution from the Cr atoms becomes negative. These results suggest that Cr atoms play a crucial role in enhancing PMA.

To explore the variation of T_C under biaxial strain, we utilized the Heisenberg model to estimate the T_C of the ML O-CrS_2. In Fig. 4(d), the T_C linearly increases, with values ranging from 800 K to 1020 K when the biaxial strain ranges from –5% to 5%. This observation aligns with our expectations, as previous research has demonstrated that Cr compounds typically exhibit higher T_C, such as $CrTe_2$ [32, 33] and CrX_2 (X = S/Se/Te) [42]. Hence, the imposition of biaxial strain results in distortion of the lattice structure, altering the overlap between atomic orbits. This change significantly impacts the exchange interactions among electrons, leading to an increase in the T_C. In Supplementary Materials Table S3, we observed that μ_{Cr} is significantly larger than μ_S, and both increase monotonically as the biaxial strain intensi-

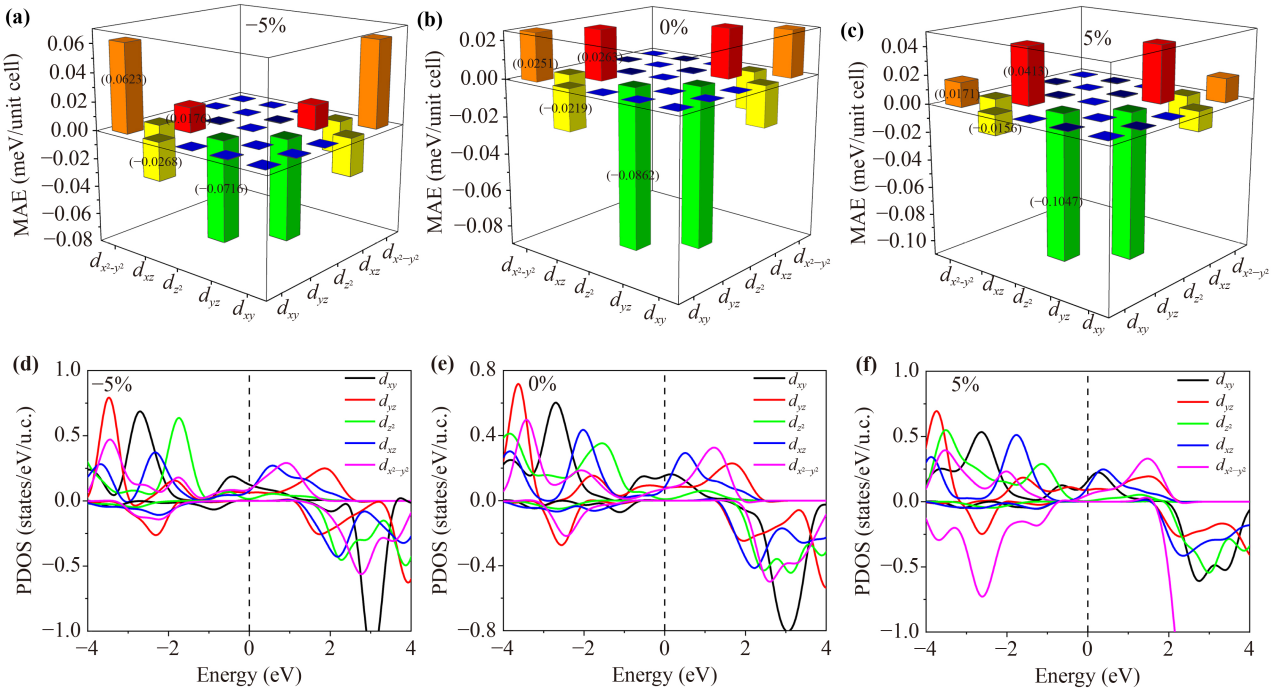

Fig. 5 The MAE mechanism analysis of ML O-CrS_2. Orbital-resolved MAE of Cr atoms at **(a)** –5% compressive strain, **(b)** 0% unstrain, and **(c)** 5% tensile strain. Projected density of states of Cr atoms' 3d orbit at **(d)** –5% compressive strain **(e)** 0% unstrain, and **(f)** 5% tensile strain.

fies. Therefore, ML O-CrS_2 exhibits considerable potential for application in spin valves, information transmission, and storage between electrical and spin signals.

3.5 Mechanistic analysis of the magnetic anisotropy

According to second-order perturbation theory [52],

$$MAE = \beta\xi^2 \sum_{o,u} \frac{\left|\left\langle \Psi_o \left| \hat{L}_z \right| \Psi_u \right\rangle\right|^2 - \left|\left\langle \Psi_o \left| \hat{L}_x \right| \Psi_u \right\rangle\right|^2}{E_u - E_o}. \tag{3}$$

Here, β represents the spin–orbit coupling parameter of Cr atoms, and $E_u - E_o$ represents the energy difference between the unoccupied (u) state and the occupied state (o), which is inversely proportional to the MAE. $|\langle\Psi_o|\hat{L}_z|\Psi_u\rangle|^2 - |\langle\Psi_o|\hat{L}_x|\Psi_u\rangle|^2$ represents the spin–orbit angular momentum matrix elements.

To investigate the influence of biaxial strain on the PMA mechanism in ML O-CrS_2, we selected strain values of –5%, 0%, and 5% as representative. The orbital-resolved MAE is depicted in Figs. 5(a)–(c). For Cr atoms under strain values of –5%, it can be observed that the hybridization between d_{z^2} with d_{yz} [green bars in Fig. 5(a)] and d_{xz} with d_{xy} (yellow bars) results in PMA contributions. Conversely, the hybridization between $d_{x^2-y^2}$ with d_{xy} (orange bars) and d_{yz} with d_{xz} (red bars) forms a robust In-Plane Magnetic Anisotropy (IMA). The relatively small amplitude of Cr's anisotropy in ML O-CrS_2 is attributed to the competition between two types of hybridizations. The variations in MAE amplitudes when the Cr atoms interact with S atoms are presented in Fig. 5(c). Here, PMA continues to increase (green bars), while IMA decreases (orange bars), leading to a weakening of IMA in the Cr atom. When the strain reaches 0% as shown in Fig. 5(b), the PMA (green bars) and IMA (orange bars) increase, resulting in an enhancement of PMA in Cr atoms.

Next, we delve into how the electronic states of the Cr-3d orbitals influence the MAE. Fundamentally, the MAE is mainly influence by the SOC effect. In Figs. 5(d)–(f), the occupied and unoccupied electronic states of Cr-3d orbitals around the Femi level are predominantly spin-up channels. The peaks of the d_{xy}, d_{xz}, and d_{z^2} states near the Femi level decrease, indicating that the d_{yz} and $d_{x^2-y^2}$ states at deeper energy levels contribute more significantly to the MAE. Consequently, the amplitude of PMA of ML O-CrS_2 from hybridization decreases at a –5% compressive strain. When a tensile strain of 5% is applied, the density of states d_{xy} and d_{xz} becomes more delocalized, leading to a continued decrease in the amplitude of PMA from hybridization. However, the d_{yz} and $d_{x^2-y^2}$ states of Cr move closer to the Femi level and become more localized [Fig. 5(e)], resulting in an enhancement of IMA led by the hybridization. In summary, biaxial strain can modulate electronic states of Cr atoms close to ML O-CrS_2, thereby effectively enhancing its PMA.

4 Conclusion

By using the DFT method, we have computed a novel 2D ML O-CrS_2 material. This material exhibits dynamic, thermodynamic, and mechanical stability. The ML O-CrS_2 is an FM with a T_C of 895 K in the unstrained state. The electronic structure reveals that it is a spin-up channel half-metallicity and displays significant out-of-plane magnetic anisotropy of 0.034 meV/Cr in the FM state. Additionally, we explored the magnetic properties of the ML O-CrS_2 under biaxial strain ranging from –5% to 5%. The system consistently exhibits FM and half-metallicity, with a T_C consistently above room temperature. We have scrutinized the orbital- (atom-) resolved MAE and PDOS and ultimately discovered that the microscopically strong PMA originates from the alteration of Cr atoms' electronic state. The negative contribution of the MAE is suppressed by compressive strain. Therefore, ML O-CrS_2 emerges as a potential candidate for future nanoelectronic applications and warrants further exploration in subsequent experiments.

Declarations The authors declare that they have no competing interests and there are no conflicts.

Data availability statement All data that support the findings of this study are included within the article (and any supplementary materials).

Electronic supplementary materials The online version contains supplementary material available at https://doi.org/10.1007/s11467-023-1387-y and https://journal.hep.com.cn/fop/EN/10.1007/s11467-023-1387-y.

Acknowledgements This work was financially supported by the Key Project of the Natural Science Program of Xinjiang Uygur Autonomous Region (Grant No. 2013D01D03), the National Natural Science Foundation of China (Grant Nos. 52073308 and 12004439), the Central South University Research Fund for Sheng Hua Scholars (Grant No. 502033019), Hunan Provincial Innovation Foundation for Postgraduate (Grant No. CX20190107), the State Key Laboratory of Powder Metallurgy at Central South University, the Fundamental Research Funds for the Central Universities of Central South University, the Tianchi-Talent Project for Young Doctors of Xinjiang Uygur Autonomous Region (No. 51052300570), the National Science Foundation of Hunan Province (No. 2021JJ30864), the Key Project of the Natural Science Program of Xinjiang Uygur Autonomous Region (Grant No. 2023D01D03), and the Outstanding Doctoral Student Innovation Project of Xinjiang University (No. XJU2023BS028). This work was carried out in part using computing resources at the High Performance Computing Center of Central South University.

References

1. K. S. Novoselov, A. K. Geim, S. V. Morozov, D. Jiang, M. I. Katsnelson, I. V. Grigorieva, S. V. Dubonos, and A. A. Firsov, Two-dimensional gas of massless Dirac fermions in graphene, *Nature* 438(7065), 197 (2005)
2. D. Golberg, Y. Bando, Y. Huang, T. Terao, M. Mitome, C. C. Tang, and C. Y. Zhi, Boron nitride nanotubes and nanosheets, *ACS Nano* 4(6), 2979 (2010)
3. Q. H. Wang, K. Kalantar-Zadeh, A. Kis, J. N. Coleman, and M. S. Strano, Electronics and optoelectronics of two-dimensional transition metal dichalcogenides, *Nat. Nanotechnol.* 7(11), 699 (2012)
4. M. S. Xu, T. Liang, M. M. Shi, and H. Z. Chen, Graphene-like two-dimensional materials, *Chem. Rev.* 113(5), 3766 (2013)
5. H. Liu, A. T. Neal, Z. Zhu, Z. Luo, X. Xu, D. Tománek, and P. D. Ye, Phosphorene: An unexplored 2D semiconductor with a high hole mobility, *ACS Nano* 8(4), 4033 (2014)
6. J. C. Lei, X. Zhang, and Z. Zhou, Recent advances in MXene: Preparation, properties, and applications, *Front. Phys.* 10(3), 276 (2015)
7. N. D. Mermin and H. Wagner, Absence of ferromagnetism or antiferromagnetism in one- or two-dimensional isotropic Heisenberg models, *Phys. Rev. Lett.* 17(22), 1133 (1966)
8. H. H. Kim, B. W. Yang, S. W. Li, S. W. Jiang, C. H. Jin, Z. Tao, G. Nichols, F. Sfigakis, S. Z. Zhong, C. H. Li, S. J. Tian, D. G. Cory, G. X. Miao, J. Shan, K. F. Mak, H. C. Lei, K. Sun, L. Y. Zhao, and A. W. Tsen, Evolution of interlayer and intralayer magnetism in three atomically thin chromium trihalides, *Proc. Natl. Acad. Sci. USA* 116(23), 11131 (2019)
9. B. Huang, G. Clark, D. R. Klein, D. MacNeill, E. Navarro-Moratalla, K. L. Seyler, N. Wilson, M. A. McGuire, D. H. Cobden, D. Xiao, W. Yao, P. Jarillo-Herrero, and X. Xu, Electrical control of 2D magnetism in bilayer CrI_3, *Nat. Nanotechnol.* 13(7), 544 (2018)
10. H. B. Wang, F. R. Fan, S. S. Zhu, and H. Wu, Doping enhanced ferromagnetism and induced half-metallicity in CrI_3 monolayer, *Europhys. Lett.* 114(4), 47001 (2016)
11. Y. J. Deng, Y. J. Yu, Y. C. Song, J. Z. Zhang, N. Z. Wang, Z. Y. Sun, Y. F. Yi, Y. Z. Wu, S. W. Wu, J. Y. Zhu, J. Wang, X. H. Chen, and Y. B. Zhang, Gate-tunable room-temperature ferromagnetism in two-dimensional Fe_3GeTe_2, *Nature* 563(7729), 94 (2018)
12. Z. X. Shen, X. Y. Bo, K. Cao, X. G. Wan, and L. X. He, Magnetic ground state and electron-doping tuning of Curie temperature in Fe_3GeTe_2: First-principles studies, *Phys. Rev. B* 103(8), 085102 (2021)
13. C. Gong, L. Li, Z. L. Li, H. W. Ji, A. Stern, Y. Xia, T. Cao, W. Bao, C. Z. Wang, Y. Wang, Z. Q. Qiu, R. J. Cava, S. G. Louie, J. Xia, and X. Zhang, Discovery of intrinsic ferromagnetism in two-dimensional van der Waals crystals, *Nature* 546(7657), 265 (2017)
14. A. O'Neill, S. Rahman, Z. Zhang, P. Schoenherr, T. Yildirim, B. Gu, G. Su, Y. R. Lu, and J. Seidel, Enhanced room temperature ferromagnetism in highly strained 2D semiconductor $Cr_2Ge_2Te_6$, *ACS Nano* 17(1), 735 (2023)
15. B. Huang, G. Clark, E. Navarro-Moratalla, D. R. Klein, R. Cheng, K. L. Seyler, D. Zhong, E. Schmidgall, M. A. McGuire, D. H. Cobden, W. Yao, D. Xiao, P. Jarillo-

Herrero, and X. Xu, Layer-dependent ferromagnetism in a van der Waals crystal down to the monolayer limit, *Nature* 546(7657), 270 (2017)
16. D. J. O'Hara, T. Zhu, A. H. Trout, A. S. Ahmed, Y. K. Luo, C. H. Lee, M. R. Brenner, S. Rajan, J. A. Gupta, D. W. McComb, and R. K. Kawakami, Room temperature intrinsic ferromagnetism in epitaxial manganese selenide films in the monolayer limit, *Nano Lett.* 18(5), 3125 (2018)
17. R. A. de Groot, F. M. Mueller, P. G. Engen, and K. H. J. Buschow, New class of materials: Half-metallic ferromagnets, *Phys. Rev. Lett.* 50(25), 2024 (1983)
18. S. Q. Zhang, R. Z. Xu, W. H. Duan, and X. L. Zou, Intrinsic half-metallicity in 2D ternary chalcogenides with high critical temperature and controllable magnetization direction, *Adv. Funct. Mater.* 29(14), 1808380 (2019)
19. G. J. Zhang, F. Guo, H. Wu, X. K. Wen, L. Yang, W. Jin, W. F. Zhang, and H. X. Chang, Above-room-temperature strong intrinsic ferromagnetism in 2D van der Waals Fe_3GaTe_2 with large perpendicular magnetic anisotropy, *Nat. Commun.* 13(1), 5067 (2022)
20. F. J. J. Han, X. Yan, F. Li, H. Yu, W. J. Li, X. Zhong, A. Bergara, and G. C. Yang, Prediction of monolayer FeP_4 with intrinsic half-metal ferrimagnetism above room temperature, *Phys. Rev. B* 107(2), 024414 (2023)
21. M. R. Habib, S. P. Wang, W. J. Wang, H. Xiao, S. M. Obaidulla, A. Gayen, Y. Khan, H. Z. Chen, and M. S. Xu, Electronic properties of polymorphic two-dimensional layered chromium disulphide, *Nanoscale* 11(42), 20123 (2019)
22. X. Sun, W. Li, X. Wang, Q. Sui, T. Zhang, Z. Wang, L. Liu, D. Li, S. Feng, S. Zhong, H. Wang, V. Bouchiat, M. Nunez Regueiro, N. Rougemaille, J. Coraux, A. Purbawati, A. Hadj-Azzem, Z. Wang, B. Dong, X. Wu, T. Yang, G. Yu, B. Wang, Z. Han, X. Han, and Z. Zhang, Room temperature ferromagnetism in ultra-thin van der Waals crystals of 1T-$CrTe_2$, *Nano Res.* 13(12), 3358 (2020)
23. L. J. Meng, Z. Zhou, M. Q. Xu, S. Q. Yang, K. P. Si, L. X. Liu, X. G. Wang, H. N. Jiang, B. X. Li, P. X. Qin, P. Zhang, J. L. Wang, Z. Q. Liu, P. Z. Tang, Y. Ye, W. Zhou, L. H. Bao, H. J. Gao, and Y. J. Gong, Anomalous thickness dependence of Curie temperature in air-stable two-dimensional ferromagnetic 1T-$CrTe_2$ grown by chemical vapor deposition, *Nat. Commun.* 12(1), 809 (2021)
24. Y. Z. Sun, P. F. Yan, J. Ning, X. Q. Zhang, Y. F. Zhao, Q. W. Gao, M. Kanagaraj, K. P. Zhang, J. J. Li, X. Y. Lu, Y. Yan, Y. Li, Y. B. Xu, and L. He, Ferromagnetism in two-dimensional $CrTe_2$ epitaxial films down to a few atomic layers, *AIP Adv.* 11(3), 035138 (2021)
25. X. Q. Zhang, Q. S. Lu, W. Q. Liu, W. Niu, J. B. Sun, J. Cook, M. Vaninger, P. F. Miceli, D. J. Singh, S. W. Lian, T. R. Chang, X. Q. He, J. Du, L. He, R. Zhang, G. Bian, and Y. B. Xu, Room-temperature intrinsic ferromagnetism in epitaxial $CrTe_2$ ultrathin films, *Nat. Commun.* 12(1), 2492 (2021)
26. X. H. Deng and Z. Y. Li, Intrinsic ultra-wide completely spin-polarized state realized in a new CrO_2 monolayer, *Phys. Chem. Chem. Phys.* 22(30), 17038 (2020)
27. B. W. Zhang, J. Sun, J. C. Leng, C. Zhang, and J. Wang, Tunable two dimensional ferromagnetic topological half-metal CrO_2 by electronic correction and spin direction, *Appl. Phys. Lett.* 117(22), 222407 (2020)
28. X. H. Tian and J. M. Zhang, The electronic, magnetic and optical properties of single-layer CrS_2 with vacancy defects, *J. Magn. Magn. Mater.* 487, 165300 (2019)
29. K. Y. Chen, J. K. Deng, Y. Yan, Q. Shi, T. Y. Chang, X. D. Ding, J. Sun, S. Yang, and J. Z. Liu, Diverse electronic and magnetic properties of CrS_2 enabling strain-controlled 2D lateral heterostructure spintronic devices, *npj Comput. Mater.* 7(1), 79 (2021)
30. M. Z. Liu, Y. L. Huang, J. Gou, Q. J. Liang, R. Chua, S. S. Arramel, S. Duan, L. Zhang, L. L. Cai, X. Yu, D. Zhong, W. Zhang, and A. T. S. Wee, Duan, L. Zhang, L. L. Cai, X. J. Yu, D. Y. Zhong, W. J. Zhang, and A. T. S. Wee, Diverse structures and magnetic properties in nonlayered monolayer chromium selenide, *J. Phys. Chem. Lett.* 12(32), 7752 (2021)
31. M. Alsubaie, C. Tang, D. Wijethunge, D. C. Qi, and A. J. Du, First-principles study of the enhanced magnetic anisotropy and transition temperature in a $CrSe_2$ monolayer via hydrogenation, *ACS Appl. Electron. Mater.* 4(7), 3240 (2022)
32. Y. H. Liu, S. Kwon, G. J. de Coster, R. K. Lake, and M. R. Neupane, Structural, electronic, and magnetic properties of $CrTe_2$, *Phys. Rev. Mater.* 6(8), 084004 (2022)
33. L. L. Wu, L. W. Zhou, X. Y. Zhou, C. Wang, and W. Ji, In-plane epitaxy-strain-tuning intralayer and interlayer magnetic coupling in $CrSe_2$ and $CrTe_2$ monolayers and bilayers, *Phys. Rev. B* 106(8), L081401 (2022)
34. B. Li, Z. Wan, C. Wang, P. Chen, B. Huang, X. Cheng, Q. Qian, J. Li, Z. W. Zhang, G. Z. Sun, B. Zhao, H. F. Ma, R. X. Wu, Z. M. Wei, Y. Liu, L. Liao, Y. Ye, Y. Huang, X. D. Xu, X. D. Duan, W. Ji, and X. F. Duan, Van der Waals epitaxial growth of air-stable $CrSe_2$ nanosheets with thickness-tunable magnetic order, *Nat. Mater.* 20(6), 818 (2021)
35. A. L. Coughlin, D. Y. Xie, X. Zhan, Y. Yao, L. Z. Deng, H. Hewa-Walpitage, T. Bontke, C. W. Chu, Y. Li, J. Wang, H. A. Fertig, and S. X. Zhang, Van der Waals superstructure and twisting in self-intercalated magnet with near room-temperature perpendicular ferromagnetism, *Nano Lett.* 21(22), 9517 (2021)
36. I. H. Lee, B. K. Choi, H. J. Kim, M. J. Kim, H. Y. Jeong, J. H. Lee, S. Y. Park, Y. Jo, C. Lee, J. W. Choi, S. W. Cho, S. Lee, Y. Kim, B. H. Kim, K. J. Lee, J. E. Heo, S. H. Chang, F. Li, B. L. Chittari, J. Jung, and Y. J. Chang, Modulating curie temperature and magnetic anisotropy in nanoscale-layered Cr_2Te_3 films: Implications for room-temperature spintronics, *ACS Appl. Nano Mater.* 4(5), 4810 (2021)
37. K. Lasek, P. M. Coelho, P. Gargiani, M. Valvidares, K. Mohseni, H. L. Meyerheim, I. Kostanovskiy, K. Zberecki, and M. Batzill, Van der Waals epitaxy growth of 2D ferromagnetic $Cr_{1+\delta}Te_2$ nanolayers with concentration-tunable magnetic anisotropy, *Appl. Phys. Rev.* 9(1), 011409 (2022)
38. G. Kresse and J. Furthmüller, Efficiency of *ab-initio* total energy calculations for metals and semiconductors using a plane-wave basis set, *Comput. Mater. Sci.* 6(1), 15 (1996)

39. G. Kresse and J. Furthmuller, Efficient iterative schemes for *ab initio* total-energy calculations using a plane-wave basis set, *Phys. Rev. B* 54(16), 11169 (1996)
40. P. E. Blöchl, Projected augmented-wave method, *Phys. Rev. B* 50(24), 17953 (1994)
41. H. J. Monkhorst and J. D. Pack, Special points for Brillouin-zone integrations, *Phys. Rev. B* 13(12), 5188 (1976)
42. G. Xiao, W. Z. Xiao, Q. Chen, and L. L. Wang, Novel two-dimensional ferromagnetic materials CrX_2 (X = O, S, Se) with high Curie temperature, *J. Mater. Chem. C* 10(46), 17665 (2022)
43. A. Togo and I. Tanaka, First principles phonon calculations in materials science, *Scr. Mater.* 108, 1 (2015)
44. G. J. Martyna, M. L. Klein, and M. Tuckerman, Nosé-Hoover chains: The canonical ensemble via continuous dynamics, *J. Chem. Phys.* 97(4), 2635 (1992)
45. F. Mouhat and F. X. Coudert, Necessary and sufficient elastic stability conditions in various crystal systems, *Phys. Rev. B* 90(22), 224104 (2014)
46. L. Xiong, L. Yi, and G. Y. Gao, Search for half-metallic magnets with large half-metallic gaps in the quaternary Heusler alloys CoFeTiZ and CoFeVZ (Z = Al, Ga, Si, Ge, As, Sb), *J. Magn. Magn. Mater.* 360, 98 (2014)
47. X. T. Wang, Z. X. Cheng, J. L. Wang, L. Y. Wang, Z. Y. Yu, C. S. Fang, J. T. Yang, and G. D. Liu, Origin of the half-metallic band-gap in newly designed quaternary Heusler compounds ZrVTiZ (Z = Al, Ga), *RSC Advances* 6(62), 57041 (2016)
48. D. Soriano, M. I. Katsnelson, and J. Fernandez-Rossier, Magnetic two-dimensional chromium trihalides: A theoretical perspective, *Nano Lett.* 20(9), 6225 (2020)
49. M. Subramanian, A. Ramirez, and W. Marshall, Structural tuning of ferromagnetism in a 3D cuprate perovskite, *Phys. Rev. Lett.* 82(7), 1558 (1999)
50. W. X. Li, C. S. Guo, Q. Zang, R. Ding, and Y. Zhao, Magnetic phase transition in strained two-dimensional semiconductor MoTeI monolayer, *Appl. Surf. Sci.* 536, 147842 (2021)
51. Y. Zhu, Y. F. Pan, L. Ge, J. Y. Fan, D. N. Shi, C. L. Ma, J. Hu, and R. Q. Wu, Separating RKKY interaction from other exchange mechanisms in two-dimensional magnetic materials, *Phys. Rev. B* 108(4), L041401 (2023)
52. L. X. Kang, C. Ye, X. X. Zhao, X. Y. Zhou, J. X. Hu, Q. Li, D. Liu, C. M. Das, J. F. Yang, D. Y. Hu, J. Q. Chen, X. Cao, Y. Zhang, M. Z. Xu, J. Di, D. Tian, P. Song, G. Kutty, Q. S. Zeng, Q. D. Fu, Y. Deng, J. D. Zhou, A. Ariando, F. Miao, G. Hong, Y. Z. Huang, S. J. Pennycook, K. T. Yong, W. Ji, X. R. Wang, and Z. Liu, Phase-controllable growth of ultrathin 2D magnetic FeTe crystals, *Nat. Commun.* 11(1), 3729 (2020)
53. M. Lan, G. Xiang, Y. Nie, D. Y. Yang, and X. Zhang, The static and dynamic magnetic properties of monolayer iron dioxide and iron dichalcogenides, *RSC Adv.* 6(38), 31758 (2016)
54. G. P. Müller, M. Hoffmann, C. Disselkamp, D. Schurhoff, S. Mavros, M. Sallermann, N. S. Kiselev, H. Jonsson, and S. Blugel, Spirit: Multifunctional framework for atomistic spin simulations, *Phys. Rev. B* 99(22), 224414 (2019)
55. X. T. Fang, B. Z. Zhou, X. C. Wang, and W. B. Mi, High Curie temperature and large perpendicular magnetic anisotropy in two-dimensional half metallic OsI_3 monolayer with quantum anomalous Hall effect, *Mater. Today Phys.* 28, 100847 (2022)